NANO LETTERS

Letter

pubs.acs.org/NanoLett

Formation and Dynamics of Electron-Irradiation-Induced Defects in Hexagonal Boron Nitride at Elevated Temperatures

Thang Pham,[†,‡,∥,⊥] Ashley L. Gibb,[†,§,∥,⊥] Zhenglu Li,[†,∥] S. Matt Gilbert,[†,§,∥,⊥] Chengyu Song,[#] Steven G. Louie,[†,∥] and Alex Zettl*[,†,§,∥,⊥]

[†]Department of Physics, University of California, Berkeley, California 94720, United States

[‡]Department of Materials Science and Engineering, University of California, Berkeley, California 94720, United States

[§]Department of Chemistry, University of California, Berkeley, California 94720, United States

[∥]Materials Sciences Division, Lawrence Berkeley National Laboratory, Berkeley, California 94720 United States

[⊥]Kavli Energy NanoSciences Institute at the University of California, Berkeley and the Lawrence Berkeley National Laboratory, Berkeley, California 94720 United States

[#]The Molecular Foundry, Lawrence Berkeley National Laboratory, Berkeley, California 94720 United States

Supporting Information

ABSTRACT: The atomic structure, stability, and dynamics of defects in hexagonal boron nitride (h-BN) are investigated using an aberration-corrected transmission electron microscope operated at 80 kV between room temperature and 1000 °C. At temperatures above 700 °C, parallelogram- and hexagon-shaped defects with zigzag edges become prominent, in contrast to the triangular defects typically observed at lower temperatures. The appearance of 120° corners at defect vertices indicates the coexistence of both N- and B-terminated zigzag edges in the same defect. In situ dynamics studies show that the hexagonal holes grow by electron-induced sputtering of B−N chains, and that at high temperatures these chains can migrate from one defect corner to another. We complement the experiments with first-principles calculation which consider the thermal equilibrium formation energy of different defect configurations. It is shown that, below a critical defect size, hexagonal defects have the lowest formation energy and therefore are the more-stable configuration, and triangular defects are energetically metastable but can be "frozen in" under experimental conditions. We also discuss the possible contributions of several dynamic processes to the temperature-dependent defect formation.

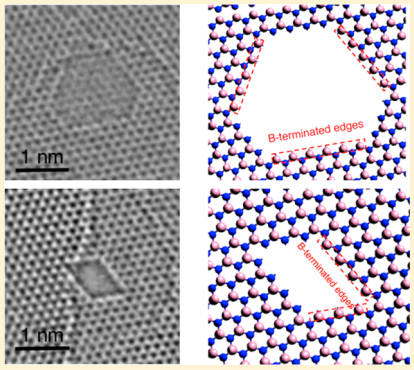

KEYWORDS: *Hexagonal boron−nitride, hexagon defect, boron-terminated edge, in situ heating, aberration-corrected transmission electron microscopy, first-principles calculations*

Monolayer graphite (i.e., graphene) has attracted significant interest over the past decade, which has in turn spurred interest in few-layer[1] and monolayer[2] h-BN. Independent of the number of layers, h-BN is a wide band gap (~5.5 eV) insulator with comparable mechanical strength to, and higher oxidation resistance than, graphene.[3] These and other characteristics make h-BN a promising candidate in various applications, such as filler for mechanically enhanced polymer composites, oxidation-resistant coatings for aerospace technologies, neutron-shielding barriers, and scaffolds for high-temperature combustion gas sensors.[4−6] As a substrate for many other 2D materials, h-BN has been shown to reduce charge density fluctuation and surface roughness, thus enhancing electronic properties in overlaid graphene[7,8] and optoelectronic properties in overlaid few-layer transitional metal dichalcogenides.[9]

Despite these novel characteristics and promising applications, the intrinsic properties of few-layer h-BN (particularly its structural properties) have not been studied as extensively as those for graphene.[10] Limited electron microscopy investigations of h-BN have revealed the atomic structure of point defects[11,12] and step edges[13] at room temperature and grain boundaries[14] at 450 °C, but analogous high-temperature (above 500 °C) defect formation, stability, and dynamics studies are very limited. The elevated-temperature atomic-scale characteristics of h-BN are critically important in understanding the physical, mechanical, and chemical properties of h-BN for future harsh-environment applications.[15]

In this report, we present an investigation of the atomic structure and dynamics of defects in h-BN using 80 kV aberration-corrected transmission electron microscopy (AC-TEM) from room temperature to 1000 °C. We find that parallelogram- and hexagon-shaped vacancies with pure zigzag edges become prominent above 700 °C. The appearance of

Received: August 15, 2016
Published: September 29, 2016

DOI: 10.1021/acs.nanolett.6b03442
Nano Lett. 2016, 16, 7142−7147

120° corners indicates the coexistence of stable long-range N- and B-terminated zigzag edges in the same defect. The stability and dynamics of these defects are also examined. Under electron-beam radiation, chains of B−N atoms are ejected from the lattice, and they can migrate from one to another region of the open defects at high temperatures. We perform first-principles calculations of the thermal equilibrium formation energy of different defects. The calculations reveal that, below a critical defect perimeter size, hexagonal defects have the lowest formation energy and therefore represent the most stable configuration. Triangular defects are in fact energetically metastable and "frozen in" under normal experimental conditions. At high temperatures (above 700 °C), the energy barrier is overcome, and the lowest-energy state (hexagonal defects) become readily accessible. Although the simple model cannot account for all of our experimental observations, it provides invaluable insight into defect stability and highlights the complexity of the real experimental conditions. We also discuss possible contributions from dynamic processes to the temperature-dependent defect formation.

Sample Preparation and Initial Characterization. h-BN samples used in this study are synthesized by a carbothermic reduction reaction between highly oriented pyrolytic graphite (HOPG) flakes, boron oxide powder, and nitrogen gas. The details of this conversion process and initial characterization (TEM, electron diffraction, EELS and Raman) can be found in the Supporting Information. Structural characterization (Figure S1) shows that the as-synthesized samples are highly crystalline few-layered h-BN with an atomic ratio of 1:1 for B and N.

Triangular Defects. Figure 1 is a representative high-resolution transmission electron microscopy (HRTEM) image of triangular defects in h-BN, obtained at 500 °C. A corresponding atomic model is also shown (B and N atoms are depicted in pink and blue, respectively) for N-terminated zigzag-edge triangles. Triangular defects of this kind are quite common in h-BN, and many of them have been previously observed at room temperatures.[2,11,16,17] The chemical composition of edge-atoms has been identified as N by high-resolution EELS and contrast comparison in scanning transmission electron microscopy (STEM) and HRTEM (N appears to have a slightly higher contrast than B).[2,16,18]

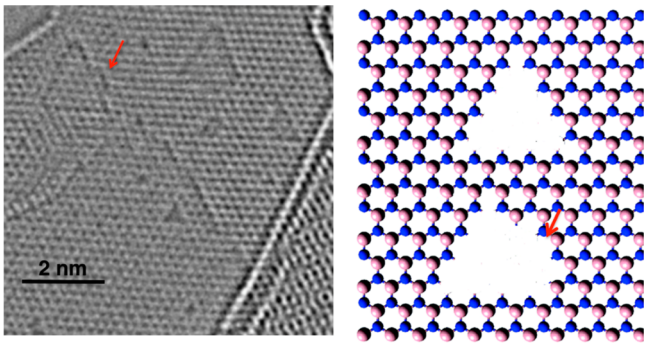

Figure 1. Representative HRTEM image of triangle defects at 500 °C (left panel) and its corresponding atomic model (right panel). The image and model also show a triangle with an ejected chain of B−N atoms (indicated by red arrows). The blue and pink spheres are N and B atoms, respectively.

The defect formation by a knock-on mechanism has been widely accepted from both experimental and theoretical studies.[11,13,16,19] As a result of the 3-fold rotational symmetry in the h-BN lattice and the asymmetry in displacement energy threshold of B and N, the defects exhibit triangular shape with exclusively N-terminated zigzag edges, i.e., B atoms are more likely to be removed first. The formation of triangular defects in h-BN that we observe at 500 °C likely originates from the same knock-on mechanism that dominates at low temperatures. Furthermore, as will be discussed in more detail below, our observations strongly suggest that the defects are enlarged by the ejection of chains of B−N atoms (and not just individual atoms), as has been suggested by Ryu et al.[18]

Hexagonal Defects. At 600 and 700 °C, we observe the appearance of hexagonal defects in addition to the conventional triangles; however, the triangular holes become unstable and very quickly (in matter of seconds during the imagining process) transform into a hexagonal configuration. Details of the stability and dynamics of defects are discussed later. At high temperatures (800, 900, and 1000 °C), the hexagonal defects with distinguishing 120° corners predominate. Figure S2 shows examples of HRTEM images of hexagonal defects at 700, 800, 900, and 1000 °C.

Warner et al.[17] have observed a minority of nontriangular (polygon) defects at room temperature (compared to the dominance of triangle defects) in h-BN, and Cretu et al.[20] have inferred that, under low-electron-acceleration voltage (30 and 60 kV), hexagonal vacancies exclusively with armchair edges are prevalent at high temperatures (above 800 °C). These researchers have attributed the defect formation to both elastic and inelastic interactions between the irradiation electron beam and the material.

Our atomic-resolution TEM study provides direct, clear, and unambiguous identification of the edge structure of the hexagonal defects (for example, at 900 °C in Figure S2). Figure 2 shows additional data recorded at 900 °C. The upper image shows a hexagonal defect, while the lower image shows a parallelogram defect. Indeed, at all temperatures studied, we find that all the edges in both cases adopt a zigzag

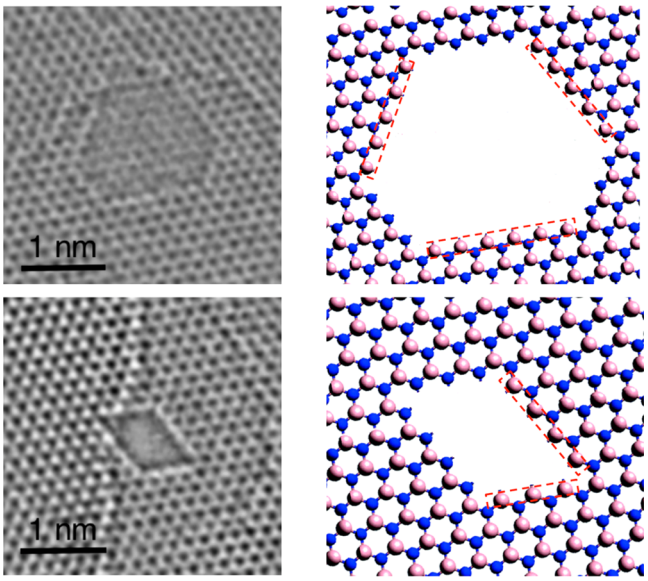

Figure 2. HRTEM images of hexagonal and parallelogram-shaped defects (at 900 °C), showing the presence of both N- and B-terminated zigzag edges in the same defect. Blue and pink spheres represent for N and B atoms, respectively. Long-range B-terminated zigzag edges are indicated by red-dotted boxes.

DOI: 10.1021/acs.nanolett.6b03442
Nano Lett. 2016, 16, 7142−7147

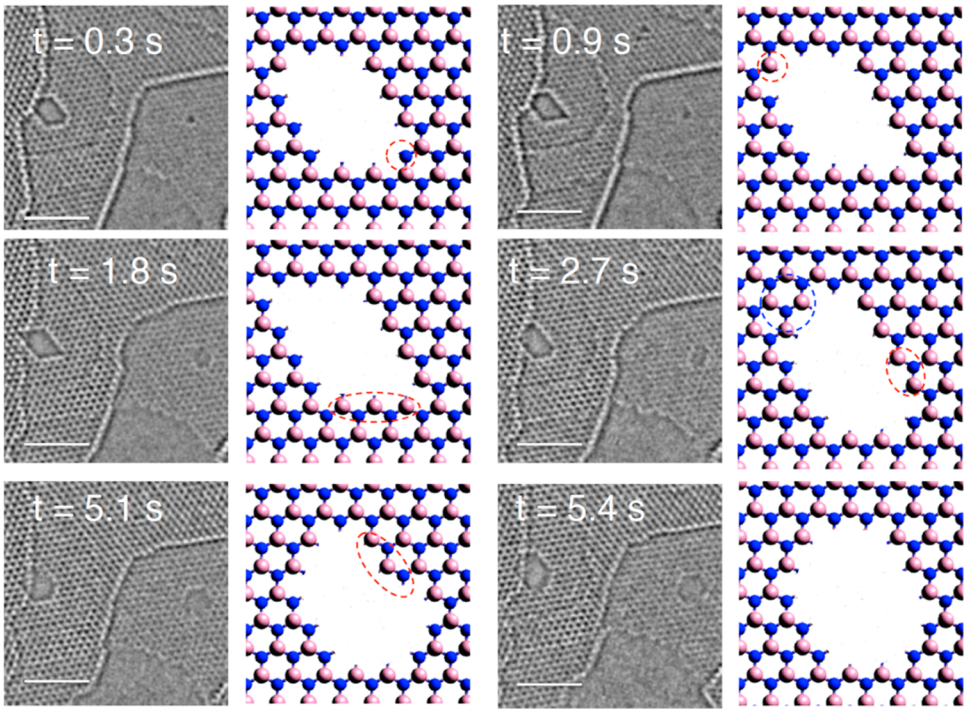

Figure 3. Stability and dynamics of a polygon defect at 900 °C. The red dotted circle indicates the atoms or chains of atoms that will be removed in the next time frame, while the blue circle indicates newly added atom(s). Scale bars are 2 nm.

configuration. The simple h-BN atomic models shown in the right panels of Figure 2 demonstrate that parallelogram and hexagon-shaped defects (or in general any defects with 120° corners) with zigzag edges must have both N- and B-terminated atoms.

This key observation apparently contradicts literature wisdom because the presence of a B-terminated zigzag edge has historically been considered possible only as an intermediate transient construct when the trianglular defects grow.[12,19] Notably, Cretu et al.[21] recently observed N monovacancies and B-terminated tetravacancies in h-BN using STEM at 500 °C, although no conclusive formation mechanism was provided. Defects in h-BN in the literature have either all N-terminated or all B-terminated edges. We also find that extended B-terminated zigzag edges are stable (at least for several seconds under imaging conditions) and ubiquitous (Figure 2), and both N-terminated and B-terminated edges coexist in the same defect.

Stability and Dynamics of Polygon Defects. We first investigate the stability and dynamics of hexagonal defects. Figure 3 shows selected 900 °C HRTEM images and their corresponding atomic models, which show the structural evolution of a polygon vacancy over time. The red dotted circle indicates an atom or chain(s) of atoms, which disappears in the following time frame, while the blue circle indicates newly added atoms. We note that for the images in Figure 2 and 3, B and N are on an equal footing and can be generally interchanged without losing the generic nature of the observation and conclusion. In other words, the blue and pink spheres can be, respectively, B and N or vice versa. Our observations suggest that parallelogram and hexagonal vacancies (or in general any zigzag edge with 120° corners) will always have both blue and pink-terminated (i.e., B and N-terminated) zigzag edges.

The initial polygon defect shown in Figure 3 is stable for 0.6 s, before the first atoms are knocked-out (as marked at t = 0.3 and 0.9 s) to adopt a parallelogram-shaped defect. The parallelogram hole is stable for 0.9 s and after that (at t = 2.7 s), a chain of B−N atoms is removed (red dotted circle) while a cluster of 4 B−N atoms is added (blue dotted circle). Because this structural reconstruction happens at high temperature (900 °C), the healing of the defect (at the top corner as marked by blue dotter circle at t = 2.7 s in Figure 3) can be realized by the migration of the removed atoms from the same defect (marked by red dotted circle at t = 1.8 s) or ejected atoms from the nearby step edges. The trapezoid defect is stable for 2.4 s (from t = 2.7 to t = 5.1 s) before chains of B−N atoms are removed at t = 5.1 and t = 5.4 s to adopt a hexagonal shape. It is interesting to note that in the nearby monolayer area there is another defect, and over time, this defect also evolves into a hexagon (see the frame at t = 5.4 s) with the same orientation.

Figure S3 and S4 show other examples of possible ejections of groups of B−N atoms during the formation of hexagon defects. More evidence is provided in Movie 3 and 4, in which we investigate the propagation of growth fronts of polygon defects at 1000 °C. The defects grow in a manner that retains the overall 120° angles at defect corners by ejecting out a single row or rows of atoms at a time. Occasionally, we observed 5|7 topographic defects at the edges of the holes. However, due to the unfavorable nature of this defect and the fast dynamics occurring at the edges, these defects usually exist in one frame and then either relax back to six-member rings or are ejected (Figure S5).

Defect Formation Mechanism From Thermal Equilibrium Considerations. To gain insight into the defect formation mechanism, we perform first-principles calculations within the density functional theory using the Quantum Espresso package[22] and compute the formation enthalpy ΔH[23] of each defect structure (triangles and hexagons).

DOI: 10.1021/acs.nanolett.6b03442
Nano Lett. 2016, 16, 7142−7147

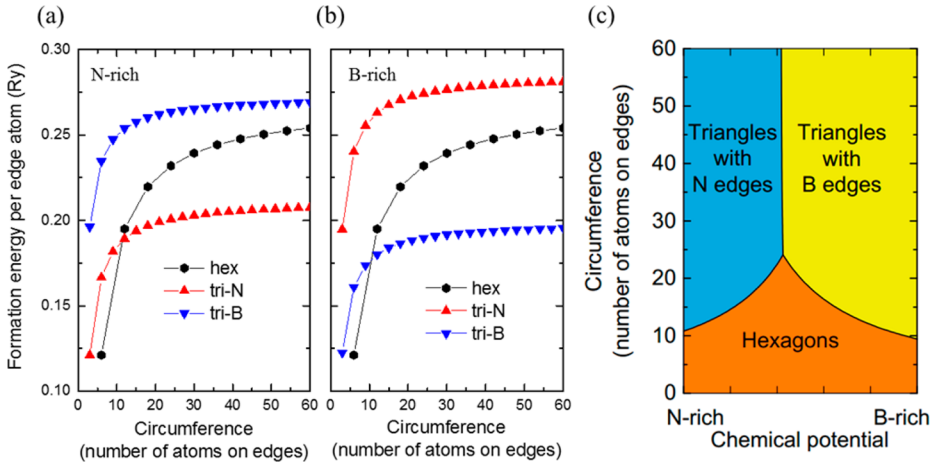

Figure 4. (a) Formation energy per unit length (occupied by one atom) as a function of circumference (i.e., number of atoms on all edges) in different types of defects in the N-rich limit. We use the edge and corner energies from Table S2 and extrapolate to get the each data point. (b) Similar to (a) but under the B-rich limit. (c) Diagram of regions of preferential existence of various defects as a function of circumference versus chemical potential. Triangular and hexagonal defects phases are included. Lines separating different domains are guides for the eyes only.

Table S1 lists the calculated formation enthalpy for six defect structures with different sizes and shapes and in two limit conditions, N-rich and B-rich environments (see the Supporting Information for more details of the definition of N-rich and B-rich limits and their roles in the calculation of the formation energy ΔH). The edge and corner energies can then be approximately extracted, as shown in Table S2. We find that formation of the edges requires more energy, whereas the corners lower the energy due to the appreciable structure reconstructions at the corners, as evidenced by the relaxed structures. More importantly, the 120° BN-corner in the hexagonal defects has lower energy than either the 60° N- or B-corner in the triangular defects. With the extracted edge and corner energies in each type of defect, we can extrapolate to obtain the formation enthalpy of defects in different sizes, assuming that all other effects are negligible (Figure 4).

Figure 4a and b present the thermal equilibrium formation energy in two limits (N-rich and B-rich environments) as a function of defect circumference (i.e., perimeter). The figures show that when the defect sizes are small ($n < 10$, where n is the number of atoms on all edges of the defect), the hexagonal defects have the lowest formation energy, and when the defects are larger ($n > 10$), triangular defects (either N- or B-terminated edges) are more stable. This is in line with our finding that the formation of a hexagonal defect can lower the total energy by having the 120° BN-corners at the cost of introducing both N- and B-terminated edges. However, when the defect size is large the advantages of the corners lessen compared to the contribution of the edges to the total energy. In this case, triangular defects become energetically preferential because they have solely one type of edges.

By varying the chemical potential between two limits (N-rich and B-rich), we derive a defect shape preference diagram in terms of defect circumference and chemical potential using the defect formation energy (Figure 4c). Apparently, under any chemical potential environment, hexagonal defects have the lowest energy when the defect sizes are small ($n < 10$ in most cases). However, triangular defects are more stable at very large sizes ($n > 25$).

This simple model (considering only thermal equilibrium formation energy of defects in the ground state at $T = 0$) provides a physical mechanism for, and shows some degree of quantitative agreement with, the experimental observations. Experimentally, we observed the presence of hexagonal defects with the size (circumference) in the range of $n = 6$ (Figure S3) to $n = 26$ (Figure S2), which clearly falls within the hexagonal-defect-dominance space in the diagram (Figure 4c). However, for triangular defects, the theoretical diagram shows their prevalence only at a large size ($n > 25$); in experiments, we observe them even with $n = 3$ (single point defect) or $n = 9$ (tetravacancies) at low temperature (<500 °C). Although this admittedly oversimplified theory cannot provide a full explanation to the temperature-dependent defect formation, it gives significant insight into the energy landscape of defect stability. We speculate that the triangular defects are favorable metastable states, and at normal conditions ($T < 500$ °C), they represent a local attractor in phase space. The lowest energy state and, hence, globally, the most-stable one for small-sized defects is more likely hexagonal. We conclude that there is an energy barrier between these two states, and indeed, by heating the samples to above 700 °C, stable hexagonal defects readily emerge experimentally. This sets the energy barrier scale.

The contrast between the theoretical model and the experimental data also emphasizes the complexity of the real experimental conditions in which additional dynamic processes likely play a role in the defect formation, as discussed below.

Defect Formation Mechanism from Dynamic Consideration. We speculate on the formation mechanism for a polygon defect with both zigzag N- and B-termination edge-atoms in h-BN. The formation mechanisms may be complex, with contributions from several dynamic processes, such as etching effects from the surrounding gas environment and the interaction between the electron beam and the material (both elastic, i.e., knock-on, and inelastic interactions). At low temperature, chemical etchants (residual hydrocarbons and metal atoms)[24] could preferentially attack and remove B atoms, leaving behind exclusively N-terminated defects. High-temperature annealing could then remove those etchants from the sample, which indeed eliminates the asymmetry in chemical reactivity of B and N. Therefore, B and N would then be ejected with similar probability, resulting in both N- and B-terminated defect-edges. Additional effects from the gas environment could contribute to the stabilization of triangular defects in the presence of elements such as oxygen at the defect

DOI: 10.1021/acs.nanolett.6b03442
Nano Lett. 2016, 16, 7142−7147

edges, as considered by Huber et al.[25] Experiments performed under a controlled gas environment (e.g., using environmental TEM) would help distinguish the role the gas environment plays in the formation and stability of defects in h-BN and graphene. At high temperatures, similar mechanisms are likely at play, with additional contributions. Previous models[19,26] considered the defect formation by elastic damage at room temperature and in the range of 80−120 kV. At high temperatures, the combination of lattice vibration,[27] elastic interaction,[19] inelastic damage[20] and even kinetic effects of edge atoms caused by impact of energetic electrons[28,29] are likely contributors.

Conclusions. We have shown the formation and dynamics of hexagonal defects with both N- and B-terminated zigzag edges in h-BN at high temperatures for the first time. The formation of these hexagon defects is based in part on the ejection of bundles of atoms as seen from high spatial and temporal resolution TEM images. We performed DFT calculations, which consider only the thermal equilibrium formation energy of static defects, and they reveal that hexagonal defects are more stable than the triangular defects for small sizes ($n < 10$). However, the real experimental conditions involve many dynamic processes, including chemical etching from gas environment and elastic (knock-on) and inelastic interaction between the electron beam and the material. These factors likely compromise the equilibrium picture and thus give rise to the experimental observation of the temperature-dependent defect formation and dynamics. This systematic study about the relationship of the defect structures and temperatures introduces a feasible and accurate way to control the shapes of h-BN defects, vacancies, edges, and nanopores at the atomic level. This control provides many technological insights for future applications. In addition, the defect formation and stability of h-BN at high temperatures also has implications for h-BN-based material performance in extreme conditions.

Methods. *h-BN Synthesis.* In this study, few-layer h-BN was prepared by carbothermic reduction from highly oriented pyrolitic graphite (HOPG) flakes. More details about the experiment setup can be found in the Supporting Information and elsewhere.[30,31] The converted h-BN flakes were then sonicated in isopropanol for 30 min before being drop-cast on a TEM grid for further microscopy investigation.

TEM and in Situ Heating. Atomic resolution TEM imaging was achieved using the TEAM 0.5 microscope at 80 kV with a monochromated beam and spherical aberration correction, yielding a spatial resolution of less than 1 Å. Spherial aberration corrections were the third order, $C_3 = -8$ μm, and the fifth order, $C_5 = 5$ mm, which yielded bright atom contrast. For the in situ heating experiment, an Aduro TEM holder (Protochips, Inc.) was used. The holder allows for controlled sample heating while imaging.

Image Processing. Raw TEM images were filtered by using a bandpass filter between 1 and 100 pixels. These filtered images were then blurred out using a Gaussian blur function with a diameter of 2 pixels to enhance visual inspections.

Computational Method. First-principles calculations were performed within the density functional theory using Quantum Espresso package.[22] We used a plane wave basis set with 45 Ry cutoff, projector augmented wave pseudopotentials, and the local density approximation.[32] We fully relaxed the lattice vectors and internal coordinates of pristine monolayer BN with a 10 Å vacuum separation between layers in adjacent cells, on the basis of which we constructed the defect structures in supercells in such a way that the defect−defect distance in the periodic image is larger than 9 Å. More details about the simulation can be found in the Supporting Information.

■ ASSOCIATED CONTENT

Supporting Information

The Supporting Information is available free of charge on the ACS Publications website at DOI: 10.1021/acs.nanolett.6b03442.

Details of h-BN synthesis, initial characterization, observation of hexagonal defects at different temperatures, dynamics of a hexagon defect, topological defects at the inner edges, and first-principles calculations. Images showing TEM results of as-prepared h-BN flakes, HRTEM results of hexagonal defects, and the time evolution of atomic structure of a hexagon defect at 900 °C. Tables showing defect structures calculated in this work and their formation enthalpies ΔH under two chemical potential limits and calculated formation enthalpies for edges and corners in different defect types. (PDF)

A video showing time evolution and dynamics of defects at 500 °C (AVI)

A video showing time evolution and dynamics of defects at 900 °C (AVI)

A video showing time evolution and dynamics of defects at 1000 °C (AVI)

A video showing time evolution and dynamics of defects at 1000 °C (AVI)

■ AUTHOR INFORMATION

Corresponding Author

*E-mail: azettl@berkeley.edu.

Author Contributions

T.P. and A.L.G. contributed equally. T.P., A.L.G., and M.G. synthesized the materials and prepared TEM samples. T.P. and A.L.G. carried out TEM study. T.P. analyzed the data. Z.L. and S.G.L. performed the theoretical analysis. S.G.L. and A.Z. supervised the project. The manuscript was written by all authors.

Notes

The authors declare no competing financial interest.

■ ACKNOWLEDGMENTS

This work was supported in part by the Director, Office of Science, Office of Basic Energy Sciences, Materials Science and Engineering Division, of the U.S. Department of Energy under contract no. DE-AC02- 05CH11231 within the sp^2-bonded Materials Program (KC2207), which provided for student support, Raman spectroscopy, and density functional calculations, and TEM characterization at the Molecular Foundry; the Defense Threat Reduction Agency under grant no. 3044-018968, which provided for student support and image analysis; the Air Force Office of Scientific Research under grant no. FA9950-14-1-0323, which provided for h-BN synthesis; and the National Science Foundation under grant no. DMR-1508412, which provided the formation energy and phase diagram analysis. Computational resources have also been provided by Stampede in Texas Advanced Computing Center. A.L.G. and S.M.G. acknowledge support from NSF graduate research fellowships.

DOI: 10.1021/acs.nanolett.6b03442
Nano Lett. 2016, 16, 7142−7147

REFERENCES

(1) Pacilé, D.; Meyer, J. C.; Girit, C. O.; Zettl, A. *Appl. Phys. Lett.* **2008**, *92* (13), 133107.
(2) Alem, N.; Erni, R.; Kisielowski, C.; Rossell, M. D.; Gannett, W.; Zettl, A. *Phys. Rev. B: Condens. Matter Mater. Phys.* **2009**, *80* (15), 155425.
(3) Cohen, M. L.; Zettl, A. *Phys. Today* **2010**, *63* (11), 34−38.
(4) Golberg, D.; Bando, Y.; Huang, Y.; Terao, T.; Mitome, M.; Tang, C.; Zhi, C. *ACS Nano* **2010**, *4* (6), 2979−2993.
(5) Fathalizadeh, A.; Pham, T.; Mickelson, W.; Zettl, A. *Nano Lett.* **2014**, *14* (8), 4881−4886.
(6) Harley-Trochimczyk, A.; Pham, T.; Chang, J.; Chen, E.; Worsley, M. A.; Zettl, A.; Mickelson, W.; Maboudian, R. *Adv. Funct. Mater.* **2015**, *26* (3), 314 DOI: 10.1002/adfm.201670017.
(7) Gannett, W.; Regan, W.; Watanabe, K.; Taniguchi, T.; Crommie, M. F.; Zettl, A. *Appl. Phys. Lett.* **2011**, *98* (24), 242105.
(8) Dean, C. R.; Young, A. F.; Meric, I.; Lee, C.; Wang, L.; Sorgenfrei, S.; Watanabe, K.; Taniguchi, T.; Kim, P.; Shepard, K. L.; Hone, J. *Nat. Nanotechnol.* **2010**, *5* (10), 722−726.
(9) Lee, G.-H.; Cui, X.; Kim, Y. D.; Arefe, G.; Zhang, X.; Lee, C.-H.; Ye, F.; Watanabe, K.; Taniguchi, T.; Kim, P.; Hone, J. *ACS Nano* **2015**, *9* (7), 7019−7026.
(10) Rasool, H. I.; Ophus, C.; Zettl, A. *Adv. Mater.* **2015**, *27* (38), 5771−5777.
(11) Meyer, J. C.; Chuvilin, A.; Algara-Siller, G.; Biskupek, J.; Kaiser, U. *Nano Lett.* **2009**, *9* (7), 2683−2689.
(12) Alem, N.; Erni, R.; Kisielowski, C.; Rossell, M. D.; Hartel, P.; Jiang, B.; Gannett, W.; Zettl, A. *Phys. Status Solidi RRL* **2011**, *5* (8), 295−297.
(13) Kim, J. S.; Borisenko, K. B.; Nicolosi, V.; Kirkland, A. I. *ACS Nano* **2011**, *5* (5), 3977−3986.
(14) Gibb, A. L.; Alem, N.; Chen, J.-H.; Erickson, K. J.; Ciston, J.; Gautam, A.; Linck, M.; Zettl, A. *J. Am. Chem. Soc.* **2013**, *135* (18), 6758−6761.
(15) Lin, Y.; Connell, J. W. *Nanoscale* **2012**, *4* (22), 6908−6939.
(16) Jin, C.; Lin, F.; Suenaga, K.; Iijima, S. *Phys. Rev. Lett.* **2009**, *102* (19), 195505.
(17) Warner, J. H.; Rümmeli, M. H.; Bachmatiuk, A.; Büchner, B. *ACS Nano* **2010**, *4* (3), 1299−1304.
(18) Ryu, G. H.; Park, H. J.; Ryou, J.; Park, J.; Lee, J.; Kim, G.; Shin, H. S.; Bielawski, C. W.; Ruoff, R. S.; Hong, S.; Lee, Z. *Nanoscale* **2015**, *7* (24), 10600−10605.
(19) Kotakoski, J.; Jin, C. H.; Lehtinen, O.; Suenaga, K.; Krasheninnikov, A. V. *Phys. Rev. B: Condens. Matter Mater. Phys.* **2010**, *82* (11), 113404.
(20) Cretu, O.; Lin, Y.-C.; Suenaga, K. *Micron* **2015**, *72*, 21−27.
(21) Cretu, O.; Lin, Y.-C.; Koshino, M.; Tizei, L. H. G.; Liu, Z.; Suenaga, K. *Phys. Rev. Lett.* **2015**, *114* (7), 075502.
(22) Giannozzi, P.; Baroni, S.; Bonini, N.; Calandra, M.; Car, R.; Cavazzoni, C.; Ceresoli, D.; Chiarotti, G. L.; Cococcioni, M.; Dabo, I.; et al. *J. Phys.: Condens. Matter* **2009**, *21* (39), 395502.
(23) Schmidt, T. M.; Baierle, R. J.; Piquini, P.; Fazzio, A. *Phys. Rev. B: Condens. Matter Mater. Phys.* **2003**, *67* (11), 113407.
(24) Ramasse, Q. M.; Zan, R.; Bangert, U.; Boukhvalov, D. W.; Son, Y.-W.; Novoselov, K. S. *ACS Nano* **2012**, *6* (5), 4063−4071.
(25) Huber, S. P.; Gullikson, E.; van de Kruijs, R. W. E.; Bijkerk, F.; Prendergast, D. *Phys. Rev. B: Condens. Matter Mater. Phys.* **2015**, *92* (24), 245310.
(26) Zobelli, A.; Gloter, A.; Ewels, C. P.; Seifert, G.; Colliex, C. *Phys. Rev. B: Condens. Matter Mater. Phys.* **2007**, *75* (24), 245402.
(27) Meyer, J. C.; Eder, F.; Kurasch, S.; Skakalova, V.; Kotakoski, J.; Park, H. J.; Roth, S.; Chuvilin, A.; Eyhusen, S.; Benner, G.; Krasheninnikov, A. V.; Kaiser, U. *Phys. Rev. Lett.* **2012**, *108* (19), 196102.
(28) Kotakoski, J.; Santos-Cottin, D.; Krasheninnikov, A. V. *ACS Nano* **2012**, *6* (1), 671−676.
(29) Zhang, Z.; Liu, Y.; Yang, Y.; Yakobson, B. I. *Nano Lett.* **2016**, *16* (2), 1398−1403.
(30) Rousseas, M.; Goldstein, A. P.; Mickelson, W.; Worsley, M. A.; Woo, L.; Zettl, A. *ACS Nano* **2013**, *7* (10), 8540−8546.
(31) Pham, T.; Goldstein, A. P.; Lewicki, J. P.; Kucheyev, S. O.; Wang, C.; Russell, T. P.; Worsley, M. A.; Woo, L.; Mickelson, W.; Zettl, A. *Nanoscale* **2015**, *7* (23), 10449−10458.
(32) Perdew, J. P.; Zunger, A. *Phys. Rev. B: Condens. Matter Mater. Phys.* **1981**, *23* (10), 5048−5079.

DOI: 10.1021/acs.nanolett.6b03442
Nano Lett. 2016, 16, 7142−7147